

Altermagnetic spin-split Fermi surfaces in CrSb revealed by quantum oscillation measurements

Taichi Terashima,^{1,*} Yuya Hattori,^{2,†} David Graf,³ Takahiro Urata,^{4,‡} Tomoki Yoshioka,⁴ Wataru Hattori,⁴ Hiroshi Ikuta,^{4,5} and Hiroaki Ikeda^{6,§}

¹*Research Center for Materials Nanoarchitectonics (MANA),
National Institute for Materials Science, Tsukuba 305-0003, Japan*

²*Center for Basic Research on Materials (CBRM),
National Institute for Materials Science, Tsukuba 305-0047, Japan*

³*National High Magnetic Field Laboratory, Florida State University, Tallahassee, Florida 32310, USA*

⁴*Department of Materials Physics, Nagoya University, Chikusa-ku, Nagoya 464-8603, Japan*

⁵*Research Center for Crystalline Materials Engineering,
Nagoya University, Chikusa-ku, Nagoya 464-8603, Japan*

⁶*Department of Physics, Ritsumeikan University, Kusatsu, Shiga 525-8577, Japan*

(Dated: January 28, 2026)

Altermagnets, a class of collinear magnets defined by their spin-split electronic bands, are a focus of intense research, where a key challenge is to experimentally verify this unique band structure as a bulk property. Here, we report a comprehensive quantum oscillation study on the prototypical altermagnet CrSb. By combining high-field magnetotransport and torque measurements with DFT+*U* calculations including spin-orbit coupling, we successfully identify a multitude of quantum-oscillation frequencies originating from four spin-non-degenerate bands. These results provide definitive, bulk-sensitive evidence for the altermagnetic spin-split Fermi surface of CrSb, which provides a firm foundation for exploring its novel electronic properties.

In nonmagnetic materials with a centrosymmetric crystal structure, the electronic bands are doubly or even-fold degenerate due to the spin degree of freedom. Ferromagnetic ordering lifts the spin degeneracy, splitting the up- and down-spin bands. In contrast, antiferromagnetic ordering is usually thought to preserve the spin degeneracy: strictly, the spin degeneracy remains if the product of the space inversion (plus a lattice translation if necessary) and the time reversal is a symmetry of the ordered state (see, for example, ref.1).

Recently, however, spin splitting and its consequences in some types of antiferromagnets have attracted much attention, partially because they might confer superior functionalities in spintronic applications. One noteworthy observation is the spontaneous anomalous Hall effect, which is usually associated with ferromagnetism, in Mn₃Sn [2] and hexagonal FeS [3]. Both compounds are antiferromagnets (the former non-collinear, the latter collinear) with vanishingly small net magnetization.

We focus on the collinear case because CrSb is a collinear antiferromagnet. Early work on FeF₂ and MnO₂ [4, 5] was followed by a flurry of theoretical studies on antiferromagnets with spin-split energy bands around 2020, including band-structure calculations, symmetry considerations, and calculations of spin current and the anomalous Hall effect [6–11]. Subsequently, the term ‘altermagnetism’ was coined for this type of antiferromagnetic ordering [12] (see [13] for a brief historical explanation). The up- and down-spin magnetic sublattices in altermagnets are connected by rotation, rather than by translation or inversion as in usual antiferromagnets. The electronic band structures of altermagnets exhibit

momentum-dependent spin splitting, which can be characterized as planar or bulk *d*-, *g*-, or *i*-waves.

RuO₂ has been identified as the prime metallic candidate for experimental verifications of altermagnetism. Theoretically predicted as an altermagnet with *d*-wave symmetry [6, 9], RuO₂ has nonetheless been confirmed as nonmagnetic in recent μ SR studies. The possible moment per Ru atom is only $\sim 10^{-4} \mu_B$ [14, 15]. Moreover, the frequencies obtained in quantum oscillation measurements on RuO₂ are consistent with the nonmagnetic state [16]. Another promising candidate is MnTe, which exhibits altermagnetic spin splitting as confirmed in angle-resolved photoemission spectroscopy (ARPES) measurements [17–19]. However, as MnTe is a semiconductor, it is unsuitable for confirming spin splitting through quantum oscillation measurements.

In contrast, CrSb is a metallic compound that crystallizes as a hexagonal NiAs-type structure in the centrosymmetric space group P6₃/mmc (#194) [inset of Fig. 1(a)]. The unit cell contains two Cr atoms connected by a 6-fold screw rotation (6₃). Neutron diffraction measurements have firmly established that one Cr is an up-spin site while the other is a down-spin site. The ordered moment in the ordered state below $T_N \sim 700$ K [20, 21] is $\sim 3\mu_B$ parallel to the *c* axis, indicating an altermagnetic order with bulk *g*-wave symmetry. Moreover, ARPES measurements have observed large *g*-wave spin-splitting of the electronic bands in CrSb [22–27]. In this work, we confirm the bulk electronic band structure with *g*-wave spin splitting through quantum oscillation measurements.

Besides altermagnetism, noncentrosymmetric crystals

or ferromagnetic materials undergo spin splitting of their electronic bands. Quantum-oscillation observations of spin-split Fermi surfaces in such cases date from the 1960s. Inversion-asymmetric splitting was first observed in HgSe [28, 29], whereas exchange-split Fermi surfaces were first studied in Fe and Ni [30–32]. To our knowledge, our present work and parallel studies in [33, 34] report the first observations of an altermagnetic spin-split Fermi surface in quantum oscillations.

CrSb single crystals were grown via two methods: the Sn-flux method and the chemical-vapor-transport (CVT) method [35, 36] (see Supplementary Material [37]). The flux-grown crystals were hexagonal rods with axes parallel to the c axis. The CVT-grown crystals were plate-shaped with surfaces perpendicular to the c axis. Accordingly, the electric currents for measuring the resistivities of the flux- and CVT-grown crystals were applied along the c and a axes, respectively. Shubnikov-de Haas (SdH) oscillations were observed in two magnet/cryostat setups: one using a 41.5-T resistive magnet and a He-3 refrigerator at the National High Magnetic Field Laboratory (NHMFL); the other using a 20-T superconducting magnet (up to 17.5 T) and a dilution refrigerator at the National Institute for Materials Science (NIMS). Consistent results were obtained from multiple samples grown via each method. This article focuses on our most thoroughly investigated samples: a flux-grown crystal with a residual resistivity ratio (RRR) of 6.8 and a CVT-grown crystal with an RRR of 9.8.

To observe Haas-van Alphen (dHvA) oscillations, we also measured magnetic torque on other flux-grown crystals using a micro cantilever at NIMS.

For the sake of data interpretation, we performed fully relativistic electronic band-structure calculations including spin-orbit coupling (SOC) using the PBE-GGA potential within the DFT (density functional theory) + U scheme with the WIEN2K code [38, 39] (see Supplemental Material [37]). SOC is essential for the data interpretation as it alters the cyclotron orbits by gapping out the crossing points of Fermi surface sheets on the nodal planes. The Fermi level is crossed by four spin-non-degenerate bands, labeled as bands-1, -2, -3, and -4 from lowest to highest energy. The corresponding Fermi surfaces are shown in Fig. 2(c). Each of the band-1 and -2 Fermi surfaces consists of an outer tubular sheet along the Γ A line and an inner closed pocket at the A point (the high-symmetry points and lines in the Brillouin zone are explained in the Supplemental Material [37]). A recent quantum-oscillation study [34] claims that the band-1 and -2 Fermi surfaces are not open along the c axis but closed, shaped like a dogbone. However, our tubular Fermi sheets are consistent with ARPES studies [23, 24, 26, 27]. The band-3 Fermi surface consists of a ring-like structure surrounding the Γ point and closed pockets at the M points, while the band-4 surface consists of ellipsoidal pockets at the M points. In the following,

the wave number k_x ($\parallel a^*$) and k_y ($k_x \perp k_y$) are measured in units of $(2/\sqrt{3})(2\pi/a)$, while k_z is measured in units of $2\pi/c$.

For instructive purposes, we briefly clarify the quantum-oscillation frequency F before presenting the data. F is related to the maximum or minimum cross-sectional area A of the Fermi surface normal to the applied field via the Onsager relation: $F = (\hbar/2\pi e)A$. The cross-sectional area A depends on where the Fermi surface is cut, which can be specified by the wave number κ along the field direction. In this context, the adjectives ‘maximum’ and ‘minimum’ refer to the A ’s at which $dA/d\kappa = 0$. The Fermi surface is determined by comparing experimental frequencies to theoretical predictions based on band-structure calculations. The temperature and magnetic-field dependences of the quantum-oscillation amplitude are described by the Lifshitz-Kosevich formula (see Supplemental Material [37]).

Figure 1 shows selected quantum-oscillation data. SdH oscillations in both the flux- and CVT-grown samples [Figs. 1(a) and 1(c)] are already discernible in the raw resistivity versus field curves and become more evident after subtracting the polynomial backgrounds. The frequencies α , β , δ , ϵ , and ζ are labeled in the Fourier transform images [Figs. 1(b), 1(d), 1(e), and 1(f)]. The ζ oscillation was most visible in the magnetic torque data [Fig. 1(f)]. The lowest frequency peaks, marked with asterisks in Figs. 1(d), 1(e), and 1(f), are neglected because they correspond to oscillations with periods of 1.5 or lower within the measured field range. Therefore, they are likely to be artifacts caused by removal of the DC component during data processing, which results in zero amplitude at zero frequency, although the peaks in Figs. 1(d) and 1(e) may include contributions from the ζ oscillation. The frequency α corresponds to F_3 in [33] and f_1 in [34], while δ corresponds to F_2 in [33]. The existence of F_1 in [33], which would yield a single oscillation period in the widest field window (24–35 T) of [33], is questionable.

Figures 2(a) and 2(b) show the field-direction dependences of the quantum-oscillation frequencies for field rotations in the ca^* and a^*a planes, respectively. In general, Fourier-transforming a high-field region (i.e., 30–41.5 T) emphasizes the high frequencies whereas Fourier-transforming a wide inverse field ($1/B$) region (i.e., 7–17.5 or 15–41.5 T) enhances the frequency resolution and better resolves the low frequencies. Figures 2(a) and 2(b) also plot the frequencies expected from the calculated Fermi surface in Fig. 2(c). For band-3, we present only the frequencies relevant to the interpretation of the experimental data (all calculated frequencies are reported in the Supplementary Material [37]).

As the field is tilted from the c axis [Fig. 2(a)], the α frequency initially decreases and thereafter increases. The increase is observed at $|\theta| > 20^\circ$, where θ is the an-

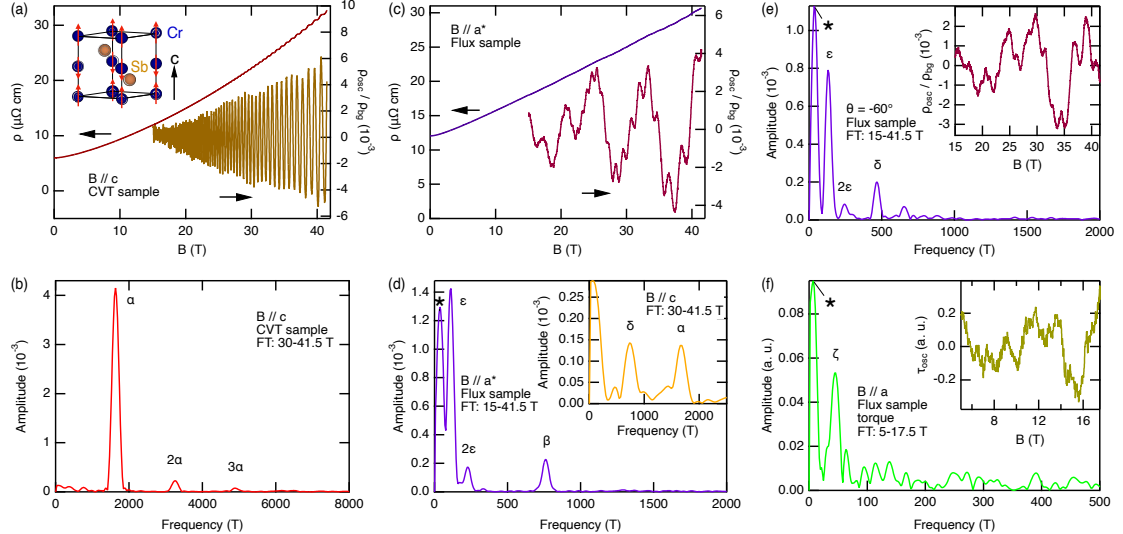


FIG. 1. Quantum oscillations in CrSb. (a) Magnetic field dependence of resistivity for $B \parallel c$ in the CVT-grown sample, along with the oscillatory component (SdH oscillations) ρ_{osc} obtained by subtracting a polynomial background ρ_{bg} . The upper-left inset shows the crystal and magnetic structures of CrSb drawn in VESTA software [40]. (b) Corresponding Fourier transform. (c) Magnetic field dependence of the resistivity for $B \parallel a^*$ in the flux-grown sample, and the SdH oscillations obtained by subtracting a polynomial background. (d) Corresponding Fourier transform and (inset) Fourier transform for $B \parallel c$ in the same flux-grown sample. (e) Fourier transform of SdH oscillations (inset) at field angle $\theta = -60^\circ$ in the flux-grown sample. θ is measured from the c axis toward the a^* axis. (f) Fourier transform of magnetic torque dHvA oscillations (inset) for $B \parallel a$. The α , β , δ , ϵ , and ζ frequency peaks are labeled in (b), (d), (e), and (f). Harmonics of α and ϵ are also indicated. The lowest frequency peaks [marked with asterisks in (d), (e), and (f)] are neglected (see text for explanation).

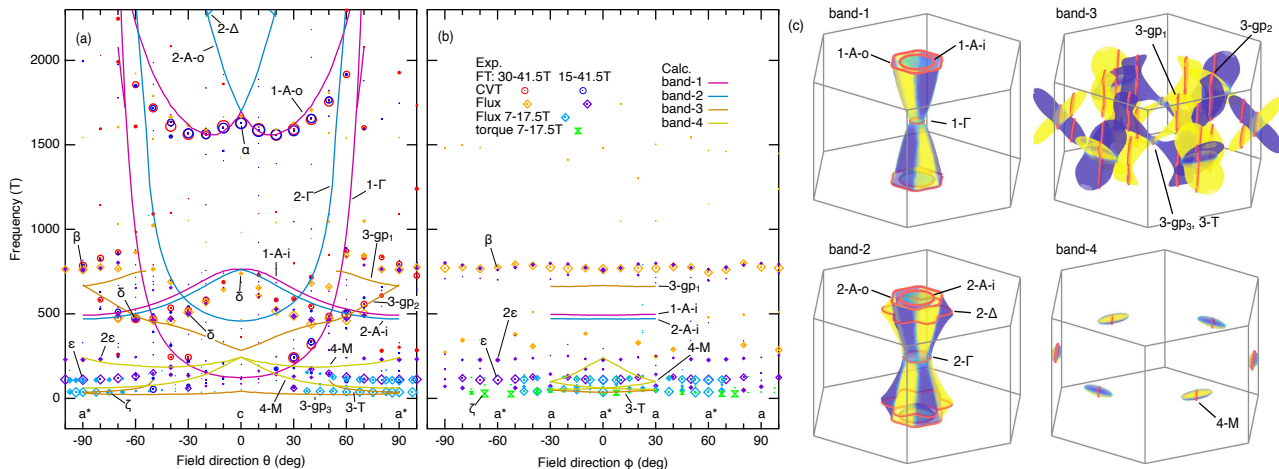


FIG. 2. Fermi surface in CrSb. Magnetic-field-direction dependences of the quantum oscillation frequencies for field rotation in the (a) ca^* and (b) a^*a planes. The experimental frequency branches are labeled with Greek letters. Different symbols correspond to different samples and/or field windows of Fourier transforms as indicated in (b), and their sizes indicate the oscillation amplitudes. The solid curves plot the theoretical frequencies calculated from the Fermi surface in (c) for $-90^\circ \leq \theta \leq 90^\circ$ (a) and $-30^\circ \leq \phi \leq 30^\circ$ (b). The attached names of the underlying orbits include the band number, orbit center, and, if necessary, inner (i) or outer (o). gp denotes a general point. (c) Fermi surface obtained from our DFT+ U calculation (with SOC). The color indicates the spin polarization s_z . Extremal orbits relevant to experimental frequencies are indicated: $B \parallel c$ for bands-1 and 2, and $B \parallel a^*$ for bands-3 and 4.

gle between the applied field and the c axis. This angular dependence can be explained by the maximum orbit at the A point of the band-1 outer tubular Fermi sheet [orbit 1-A-o in Fig. 2(c)]. In field directions near $B \parallel c$, the frequency from the minimum orbit at A of the band-2 outer tubular Fermi sheet (orbit 2-A-o) approaches the frequency of orbit 1-A-o; hence, the α oscillation includes some contribution from orbit 2-A-o. The calculated frequency 1-A-o also reasonably explains the frequency f_1 of [34] except in the immediate vicinity of $B \parallel a^*$ [37].

The authors of [33] claimed that the α oscillation (F_3 in [33]) carries a nontrivial Berry phase π . However, the oscillation phase that we determined from a Landau-fan plot (Fig. S2) does not agree with that reported in [33]. In fact, the Berry phase cannot be definitively inferred from a phase analysis of the α oscillation because the α oscillation near $B \parallel c$ is the sum of the oscillations from the two orbits (see Supplemental Material [37]).

The band-1 tubular sheet has a minimum cross-section at Γ (orbit 1- Γ), which may explain some data points such as $F \sim 240$ T at $\theta = \pm 30^\circ$ and ~ 320 T at $\pm 40^\circ$ in Fig. 2(a). The band-2 tubular sheet has a minimum cross-sections at Γ (orbit 2- Γ) and a maximum one at $k_z = 0.40$ (orbit 2- Δ). However, we find no experimental data points that clearly correspond to these orbits. The band-1 and -2 inner closed pockets at A have the maximum orbits (1-A-i and 2-A-i). These orbits may explain the δ frequency in the angular range $|\theta| \leq 30^\circ$, where the frequency decreases with $|\theta|$ [Fig. 2(a)]. However, for $|\theta| \geq 40^\circ$, δ increases with $|\theta|$. This contrasting behavior suggests that δ in this latter region should be attributed to a different orbit, as discussed below. Thus far, we have considered all possible frequencies from the band-1 and -2 Fermi sheets.

To explain the remaining frequencies, we now consider the band-3 and -4 Fermi sheets. The β frequency is not observed for $B \parallel c$ [Fig. 2(a)]. As the field is tilted toward the a^* direction, it appears at $|\theta| = 60^\circ$ and decreases with $|\theta|$. It is visible in the a^*a plane with a weak angular dependence [Fig. 2(b)]. This behavior is consistent with a maximum orbit 3-gp₁ centered at $\mathbf{k}_{\text{gp}_1} = (0.13, -0.22, 0.21)$ (and equivalent positions) on the band-3 sheet (gp means a general point) [Fig. 2(c)]. The δ frequency increases with $|\theta|$ for $|\theta| \geq 40^\circ$ [Fig. 2(a)], which can be explained by a maximum orbit 3-gp₂ centered at $\mathbf{k}_{\text{gp}_2} = (0.27, 0, 0.21)$ on the band-3 sheet. Note that the orbits 3-gp₁ and 3-gp₂ arise from symmetry-related sections of the Fermi surface [see Fig. S2]. The ϵ and ζ frequencies can be explained by orbits 4-M, 3-T, and/or 3-gp₃. The orbit 4-M is a maximum orbit on the band-4 ellipsoidal Fermi pocket at M, while the orbits 3-T and 3-gp₃ are located at a point on the T-line of the band-3 Fermi surface and a point slightly displaced from it, respectively [Fig. 2(c)].

Previous ARPES studies on CrSb have predominantly focused on bands-1 and 2 [22–26]. In contrast, our obser-

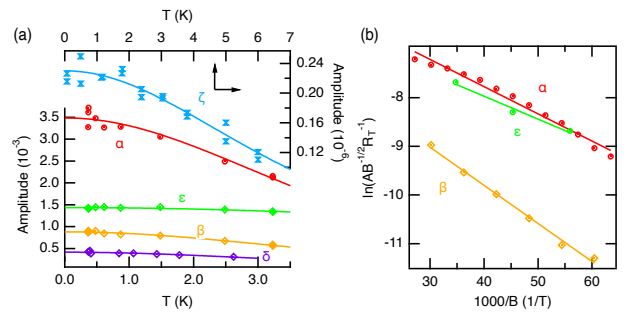


FIG. 3. Temperature and magnetic-field dependences of quantum-oscillation amplitudes in CrSb. (a) Temperature dependences of the oscillation amplitudes of α for $B \parallel c$, β and ϵ for $B \parallel a^*$, δ at $\theta = -60^\circ$, and ζ for $B \parallel a$. The solid curves are the Lifshitz–Kosevich fittings, from which the effective masses are determined. (b) Magnetic-field dependences of the oscillation amplitudes of α for $B \parallel c$ and β and ϵ for $B \parallel a^*$. The solid lines are linear fittings, from which the electron scattering times are estimated.

vation of the β and δ (for $|\theta| \geq 40^\circ$) oscillations can be assigned to the band-3 Fermi surface, providing a comprehensive experimental picture of the entire Fermi surface.

Figure 3(a) shows the temperature dependences of the oscillation amplitudes along with the Lifshitz–Kosevich fittings [37], from which the effective masses m^* were determined as follows: $m^*/m_e = 1.2(1)$ for α with $B \parallel c$, $1.23(5)$, $0.29(3)$ for β and ϵ , respectively, with $B \parallel a^*$, $0.24(1)$ for ζ with $B \parallel a$, and $1.2(2)$ for δ at $\theta = -60^\circ$. Here, m_e denotes the free electron mass. Considering that higher frequencies are thermodynamically more important than lower ones, we mention the corresponding band masses $m_{\text{band}}/m_e = 0.81$, 0.70 , and $0.96m_e$ for α , β , and δ , respectively (Table S1). The experimental effective masses are only moderately enhanced compared to these band masses ($m^*/m_{\text{band}} = 1.3$ – 1.8), suggesting that the effect of electron correlations is not strong.

Figure 3(b) shows the Dingle plots indicating the field dependences of the α , β , and ϵ oscillations, along with their linear fittings. Using the Lifshitz–Kosevich formula [37], the electron scattering times of the α , β , and ϵ oscillations were estimated from the slopes as $0.38(4)$, $0.28(2)$, and $0.11(3)$ ps, respectively, and the mobilities were estimated as $560(30)$, $400(20)$, and $700(100)$ cm²/(Vs), respectively. The mobilities exceed those reported in [33] and approximate those estimated from multicarrier analyses of the magnetotransport data of major carriers with carrier densities of 10^{20} cm⁻³ or larger [35, 36]. These multicarrier analyses suggested the existence of high-mobility minor carriers with mobilities above 2000 cm²/(Vs) and carrier densities of $\sim 10^{19}$ cm⁻³ or lower, but such carriers could not be confirmed from the present SdH measurements.

A recent theoretical work suggested that quantum-

oscillation frequencies from an altermagnet will exhibit characteristic behaviors, such as splitting of a single frequency or merging and re-splitting of two frequencies with increasing Zeeman field [41]. However, such behaviors are not observed in the present data.

In conclusion, we have performed a comprehensive quantum-oscillation study on CrSb. The altermagnetic Fermi surface predicted from our DFT+*U* calculation with SOC provides an excellent explanation for the experimentally observed quantum-oscillation frequencies. Notably, we have successfully assigned the β and δ (for $|\theta| \geq 40^\circ$) oscillations to the band-3 Fermi surface, a step that is crucial for completing the experimental picture of the entire Fermi surface. Our work thus establishes a firm, bulk-verified foundation for future investigations into the novel electronic properties of altermagnets.

This work was supported by JSPS KAKENHI Grant Numbers JP22K03537, JP23K25827, JP24KJ0227, and JP25K07202. MANA is supported by the World Premier International Research Center Initiative (WPI), MEXT, Japan. The National High Magnetic Field Laboratory is supported by National Science Foundation through NSF/DMR-2128556 and the State of Florida. TU was supported by Foundation of Public Interest of Tatematsu. We thank Troy Brumm for his valuable technical support at NHMFL. TT thanks Hisatomo Harima for valuable discussion.

Phys. **18**, 13294 (2016).

- [6] K.-H. Ahn, A. Hariki, K.-W. Lee, and J. Kuneš, Antiferromagnetism in RuO₂ as *d*-wave pomeranchuk instability, Phys. Rev. B **99**, 184432 (2019).
- [7] M. Naka, S. Hayami, H. Kusunose, Y. Yanagi, Y. Motome, and H. Seo, Spin current generation in organic antiferromagnets, Nat. Commun. **10**, 4305 (2019).
- [8] S. Hayami, Y. Yanagi, and H. Kusunose, Momentum-dependent spin splitting by collinear antiferromagnetic ordering, J. Phys. Soc. Jpn. **88**, 123702 (2019).
- [9] L. Šmejkal, R. González-Hernández, T. Jungwirth, and J. Sinova, Crystal time-reversal symmetry breaking and spontaneous Hall effect in collinear antiferromagnets, Sci. Adv. **6**, eaaz8809 (2020).
- [10] L.-D. Yuan, Z. Wang, J.-W. Luo, E. I. Rashba, and A. Zunger, Giant momentum-dependent spin splitting in centrosymmetric low-*Z* antiferromagnets, Phys. Rev. B **102**, 014422 (2020).
- [11] I. I. Mazin, K. Koepernik, M. D. Johannes, R. González-Hernández, and L. Šmejkal, Prediction of unconventional magnetism in doped FeSb₂, Proc. Natl. Acad. Sci. USA **118**, e2108924118 (2021).
- [12] L. Šmejkal, J. Sinova, and T. Jungwirth, Beyond conventional ferromagnetism and antiferromagnetism: A phase with nonrelativistic spin and crystal rotation symmetry, Phys. Rev. X **12**, 031042 (2022).
- [13] I. Mazin, Altermagnetism then and now, Physics **17**, 4 (2024).
- [14] M. Hiraishi, H. Okabe, A. Koda, R. Kadono, T. Muroi, D. Hirai, and Z. Hiroi, Nonmagnetic ground state in RuO₂ revealed by muon spin rotation, Phys. Rev. Lett. **132**, 166702 (2024).
- [15] P. Keßler, L. García-Gassull, A. Suter, T. Prokscha, Z. Salman, D. Khalyavin, P. Manuel, F. Orlandi, I. I. Mazin, R. Valentí, and S. Moser, Absence of magnetic order in RuO₂: insights from μ SR spectroscopy and neutron diffraction, npj Spintronics **2**, 50 (2024).
- [16] Z. Wu, M. Long, H. Chen, S. Paul, H. Matsuki, O. Zhelezuk, U. Zeitler, G. Li, R. Zhou, Z. Zhu, D. Graf, T. I. Weinberger, F. M. Grosche, Y. Maeno, and A. G. Eaton, Fermi surface of RuO₂ measured by quantum oscillations, Phys. Rev. X **15**, 031044 (2025).
- [17] J. Krempaský, L. Šmejkal, S. W. D’Souza, M. Hajlaoui, G. Springholz, K. Uhlířová, F. Alarab, P. C. Constantinou, V. Strocov, D. Usanov, W. R. Pudelko, R. González-Hernández, A. Birk Hellenes, Z. Jansa, H. Reichlová, Z. Šobáň, R. D. Gonzalez Betancourt, P. Wadley, J. Sinova, D. Kriegner, J. Minář, J. H. Dil, and T. Jungwirth, Altermagnetic lifting of Kramers spin degeneracy, Nature **626**, 517 (2024).
- [18] S. Lee, S. Lee, S. Jung, J. Jung, D. Kim, Y. Lee, B. Seok, J. Kim, B. G. Park, L. Šmejkal, C.-J. Kang, and C. Kim, Broken kramers degeneracy in altermagnetic MnTe, Phys. Rev. Lett. **132**, 036702 (2024).
- [19] T. Osumi, S. Souma, T. Aoyama, K. Yamauchi, A. Honma, K. Nakayama, T. Takahashi, K. Ohgushi, and T. Sato, Observation of a giant band splitting in altermagnetic MnTe, Phys. Rev. B **109**, 115102 (2024).
- [20] A. I. Snow, Neutron diffraction investigation of the atomic magnetic moment orientation in the antiferromagnetic compound CrSb, Phys. Rev. **85**, 365 (1952).
- [21] W. J. Takei, D. E. Cox, and G. Shirane, Magnetic structures in the MnSb-CrSb system, Phys. Rev. **129**, 2008 (1963).

* TERASHIMA.Taichi@nims.go.jp

† Present address: Department of Physics, Tokyo Metropolitan University, 1-1, Minami-osawa, Hachioji 192-0397, Japan

‡ urata.takahiro.k4@f.gifu-u.ac.jp; Present address: Department of Electrical, Electronic and Computer Engineering, Gifu University, Gifu, Gifu 501-1193, Japan

§ ikedah@fc.ritsumei.ac.jp

- [1] V. Cvetkovic and O. Vafek, Space group symmetry, spin-orbit coupling, and the low-energy effective Hamiltonian for iron-based superconductors, Phys. Rev. B **88**, 134510 (2013).
- [2] S. Nakatsuji, N. Kiyohara, and T. Higo, Large anomalous Hall effect in a non-collinear antiferromagnet at room temperature, Nature **527**, 212 (2015).
- [3] R. Takagi, R. Hirakida, Y. Settai, R. Oiwa, H. Takagi, A. Kitaori, K. Yamauchi, H. Inoue, J.-i. Yamaura, D. Nishio-Hamane, S. Itoh, S. Aji, H. Saito, T. Nakajima, T. Nomoto, R. Arita, and S. Seki, Spontaneous Hall effect induced by collinear antiferromagnetic order at room temperature, Nat. Mater. **24**, 63 (2025).
- [4] S. López-Moreno, A. H. Romero, J. Mejía-López, A. Muñoz, and I. V. Roshchin, First-principles study of electronic, vibrational, elastic, and magnetic properties of FeF₂ as a function of pressure, Phys. Rev. B **85**, 134110 (2012).
- [5] Y. Noda, K. Ohno, and S. Nakamura, Momentum-dependent band spin splitting in semiconducting MnO₂: a density functional calculation, Phys. Chem. Chem.

[22] S. Reimers, L. Odenbreit, L. Šmejkal, V. N. Strocov, P. Constantinou, A. B. Hellenes, R. Jaeschke Ubiergo, W. H. Campos, V. K. Bharadwaj, A. Chakraborty, T. Denneulin, W. Shi, R. E. Dunin-Borkowski, S. Das, M. Kläui, J. Sinova, and M. Jourdan, Direct observation of altermagnetic band splitting in CrSb thin films, *Nat. Commun.* **15**, 2116 (2024).

[23] G. Yang, Z. Li, S. Yang, J. Li, H. Zheng, W. Zhu, Z. Pan, Y. Xu, S. Cao, W. Zhao, A. Jana, J. Zhang, M. Ye, Y. Song, L.-H. Hu, L. Yang, J. Fujii, I. Vobornik, M. Shi, H. Yuan, Y. Zhang, Y. Xu, and Y. Liu, Three-dimensional mapping of the altermagnetic spin splitting in CrSb, *Nat. Commun.* **16**, 1442 (2025).

[24] M. Zeng, M.-Y. Zhu, Y.-P. Zhu, X.-R. Liu, X.-M. Ma, Y.-J. Hao, P. Liu, G. Qu, Y. Yang, Z. Jiang, K. Yamagami, M. Arita, X. Zhang, T.-H. Shao, Y. Dai, K. Shimada, Z. Liu, M. Ye, Y. Huang, Q. Liu, and C. Liu, Observation of spin splitting in room-temperature metallic antiferromagnet CrSb, *Adv. Sci.* **11**, 2406529 (2024).

[25] J. Ding, Z. Jiang, X. Chen, Z. Tao, Z. Liu, T. Li, J. Liu, J. Sun, J. Cheng, J. Liu, Y. Yang, R. Zhang, L. Deng, W. Jing, Y. Huang, Y. Shi, M. Ye, S. Qiao, Y. Wang, Y. Guo, D. Feng, and D. Shen, Large band splitting in *g*-wave altermagnet CrSb, *Phys. Rev. Lett.* **133**, 206401 (2024).

[26] W. Li, W. Li, M. Zou, Y. Yin, H. Li, G. Qu, Y. Huang, R. Yu, H. Yang, and B. Wang, Large anisotropic x-ray magnetic circular dichroism in altermagnetic CrSb with collinear antiferromagnetic structure at room temperature, *Phys. Rev. B* **111**, 224417 (2025).

[27] C. Li, M. Hu, Z. Li, Y. Wang, W. Chen, B. Thiagarajan, M. Leandersson, C. Polley, T. Kim, H. Liu, C. Fulga, M. G. Vergniory, O. Janson, O. Tjernberg, and J. van den Brink, Topological Weyl altermagnetism in CrSb, *Commun. Phys.* **8**, 311 (2025).

[28] C. R. Whitsett, Oscillatory magnetoresistance in mercuric selenide, *Phys. Rev.* **138**, A829 (1965).

[29] L. M. Roth, S. H. Groves, and P. W. Wyatt, Inversion asymmetry effects on oscillatory magnetoresistance in HgSe, *Phys. Rev. Lett.* **19**, 576 (1967).

[30] J. R. Anderson and A. V. Gold, de Haas-van Alphen effect and internal field in iron, *Phys. Rev. Lett.* **10**, 227 (1963).

[31] A. S. Joseph and A. C. Thorsen, de Haas-van Alphen effect and Fermi surface in nickel, *Phys. Rev. Lett.* **11**, 554 (1963).

[32] A. V. Gold, Fermi-surface studies in iron and nickel, *J. Appl. Phys.* **39**, 768 (1968).

[33] J. Du, X. Peng, Y. Wang, S. Zhang, Y. Sun, C. Wu, T. Zhou, L. Liu, H. Wang, J. Yang, B. Chen, C. Xi, Z. Jiao, Q. Wu, and M. Fang, Topological nontrivial Berry phase in altermagnet CrSb, arXiv:2509.21303 (2025).

[34] M. Long, T. I. Weinberger, Z. Wu, M. F. Hansen, R. Tao, M. Shrestha, D. Graf, Y. Skourski, F. M. Grosche, and A. G. Eaton, 3D bulk-resolved *g*-wave magnetic order parameter symmetry in the metallic altermagnet CrSb, arXiv:2601.14526 (2026).

[35] T. Urata, W. Hattori, and H. Ikuta, High mobility charge transport in a multicarrier altermagnet CrSb, *Phys. Rev. Mater.* **8**, 084412 (2024).

[36] X. Peng, Y. Wang, S. Zhang, Y. Zhou, Y. Sun, Y. Su, C. Wu, T. Zhou, L. Liu, H. Wang, J. Yang, B. Chen, Z. Fang, J. Du, Z. Jiao, Q. Wu, and M. Fang, Scaling behavior of magnetoresistance and Hall resistivity in the altermagnet CrSb, *Phys. Rev. B* **111**, 144402 (2025).

[37] See Supplemental Material at [URL] for the crystal growth procedure, Lifshitz-Kosevich formula, band-structure calculations, Landau-fan plot of α oscillations, and experimental and calculated Fermi surface parameters, which includes Refs. 38–51

[38] P. Blaha, K. Schwarz, F. Tran, R. Laskowski, G. K. H. Madsen, and L. D. Marks, WIEN2k: An APW+lo program for calculating the properties of solids, *J. Chem. Phys.* **152**, 074101 (2020).

[39] J. P. Perdew, K. Burke, and M. Ernzerhof, Generalized Gradient Approximation Made Simple, *Phys. Rev. Lett.* **77**, 3865 (1996).

[40] K. Momma and F. Izumi, VESTA3 for three-dimensional visualization of crystal, volumetric and morphology data, *J. Appl. Crystallogr.* **44**, 1272 (2011).

[41] Z.-X. Li, H. Zhou, X. Wan, and W. Chen, Diagnosing altermagnetic phases through quantum oscillations, *Phys. Rev. B* **111**, 125119 (2025).

[42] F. E. Richards, Investigation of the magnetoresistance quantum oscillations in magnesium, *Phys. Rev. B* **8**, 2552 (1973).

[43] D. Shoenberg, *Magnetic Oscillations in Metals* (Cambridge University Press, Cambridge, 1984).

[44] G. P. Mikitik and Y. V. Sharlai, Semiclassical energy levels of electrons in metals with band degeneracy lines, *Soviet Physics–JETP* **87**, 747 (1998).

[45] A. Alexandradinata and L. Glazman, Fermiology of topological metals, *Annu. Rev. Condens. Matter Phys.* **14**, 261 (2023).

[46] H. Aoki, N. Kimura, and T. Terashima, Fermi surface properties, metamagnetic transition and quantum phase transition of CeRu₂Si₂ and its alloys probed by the dHvA effect, *J. Phys. Soc. Jpn.* **83**, 072001 (2014).

[47] A. I. Liechtenstein, V. I. Anisimov, and J. Zaanen, Density-functional theory and strong interactions: Orbital ordering in Mott-Hubbard insulators, *Phys. Rev. B* **52**, R5467 (1995).

[48] A. B. Shick, A. I. Liechtenstein, and W. E. Pickett, Implementation of the LDA+U method using the full-potential linearized augmented plane-wave basis, *Phys. Rev. B* **60**, 10763 (1999).

[49] A. G. Petukhov, I. I. Mazin, L. Chioncel, and A. I. Liechtenstein, Correlated metals and the LDA + U method, *Phys. Rev. B* **67**, 153106 (2003).

[50] N. Marzari and D. Vanderbilt, Maximally localized generalized Wannier functions for composite energy bands, *Phys. Rev. B* **56**, 12847 (1997).

[51] J. Kuneš, R. Arita, P. Wissgott, A. Toschi, H. Ikeda, and K. Held, Wien2wannier: From linearized augmented plane waves to maximally localized Wannier functions, *Comput. Phys. Commun.* **181**, 1888 (2010).

Supplemental Material: Altermagnetic spin-split Fermi surfaces in CrSb revealed by quantum oscillation measurements

Taichi Terashima,^{1,*} Yuya Hattori,^{2,†} David Graf,³ Takahiro Urata,^{4,‡}
Tomoki Yoshioka,⁴ Wataru Hattori,⁴ Hiroshi Ikuta,^{4,§} and Hiroaki Ikeda^{6,§}

¹*Research Center for Materials Nanoarchitectonics (MANA),
National Institute for Materials Science, Tsukuba 305-0003, Japan*

²*Center for Basic Research on Materials (CBRM),
National Institute for Materials Science, Tsukuba 305-0047, Japan*

³*National High Magnetic Field Laboratory,
Florida State University, Tallahassee, Florida 32310, USA*

⁴*Department of Materials Physics, Nagoya University,
Chikusa-ku, Nagoya 464-8603, Japan*

⁵*Research Center for Crystalline Materials Engineering,
Nagoya University, Chikusa-ku, Nagoya 464-8603, Japan*

⁶*Department of Physics, Ritsumeikan University, Kusatsu, Shiga 525-8577, Japan*

(Dated: January 28, 2026)

CRYSTAL GROWTH

Single crystals of CrSb were grown using the Sn-flux and chemical vapor transport (CVT) methods. The Sn-flux method (see [SM1] for details) yielded hexagonal-rod-shaped crystals. Out-of-plane x-ray diffraction and transmission Laue measurements revealed that the long axis was parallel to the c axis, while the lateral facet was parallel to the $\{01\bar{1}0\}$ plane. The CVT method, performed as described in [SM2], yielded plate-like crystals with an edge angle of 120 degrees. Out-of-plane X-ray diffraction measurements of these samples confirmed that the largest facet was parallel to the (0001) plane. The in-plane crystal orientation was determined from transmission Laue measurements.

LIFSHITZ–KOSEVICH FORMULA FOR DESCRIBING SHUBNIKOV–DE HAAS OSCILLATIONS

A Shubnikov–de Haas oscillation ρ_{osc} from an extremal orbit without spin degeneracy is expressed as [SM3, SM4]

$$\frac{\rho_{osc}}{\rho_0} = -C\sqrt{B}R_T R_D \cos \left[2\pi \left(\frac{F}{B} - \frac{1}{2} \right) + \phi_D + \phi_B + \phi_Z \right], \quad (\text{S1})$$

where ρ_0 is the background resistivity, and C is a positive coefficient. Harmonics are neglected. We tacitly assumed that $\sigma = \rho/(\rho^2 + \rho_H^2) \approx \rho^{-1}$, which is valid when the Hall resistivity ρ_H is sufficiently smaller than ρ . The frequency F is related to the Fermi-surface cross-sectional area A as $F = (\hbar/2\pi e)A$. The temperature and Dingle reduction factors are given by $R_T = X/\sinh X$ and $R_D = \exp(-X_D)$, respectively, where $X_{(D)} = K\mu^*T_{(D)}/B$, $\mu^* = m^*/m_e$, and the coefficient K is 14.69 T/K.

We define three phase offsets as follows: ϕ_D is $+\pi/4$ and $-\pi/4$ when the oscillation arises from a minimum and maximum cross section, respectively. ϕ_B is the Berry phase, which is 0 for normal electrons and π for Dirac fermions [SM5, SM6]. ϕ_Z describes the phase shift due to the Zeeman energy. For a quadratic band dispersion, ϕ_Z is given by $\pi\bar{g}\mu^*/2$, where \bar{g} is an effective g factor averaged over the cyclotron orbit [SM4, SM7]. For a linear band dispersion, ϕ_Z is not constant but depends on the magnetic field.

By fitting the temperature reduction factor R_T to the experimental temperature dependence of the oscillation amplitude, one can estimate the effective mass m^* . This mass is raised above the band mass by electron–electron and electron–phonon interactions [SM4].

The Dingle temperature T_D is estimated from a plot of $\ln[A/(\sqrt{B}R_T)]$ against $1/B$, where A is the oscillation amplitude. Such a plot is called a Dingle plot [SM4]. According to the form of R_D , the Dingle plot should be linear with a slope of $-K\mu^*T_D$. The Dingle temperature T_D is inversely proportional to the carrier scattering time τ : specifically, $T_D = \hbar/2\pi k_B\tau$. Moreover, the mobility can be estimated as $\mu = e\tau/m^*$.

BAND STRUCTURE CALCULATIONS

Fully relativistic spin-polarized electronic-structure calculations including spin-orbit coupling (SOC) were performed using the WIEN2K code [SM8]. The exchange-correlation potential was treated within the generalized gradient approximation in the Perdew-Burke-Ernzerhof (PBE) form [SM9]. The electronic structure was converged using a $7 \times 7 \times 5$ k -point mesh with RKmax = 7, and the crystallographic parameters were taken from experimental data [SM10]. Space group #194 was used for the paramagnetic state, while space group #164 was used for the altermagnetic state.

Electron correlation effects were treated within the DFT+ U scheme [SM11–SM13] employing the around-mean-field (AMF) double-counting correction, with the Hubbard U applied to the Cr d orbitals. A Wannier-based tight-binding Hamiltonian was constructed using the WANNIER90 code [SM14] interfaced with WIEN2K via WIEN2KWANNIER [SM15]. Based on this Hamiltonian, the Fermi surfaces were constructed, and the quantum oscillation frequencies and cyclotron effective masses were evaluated.

Four bands cross the Fermi level. Bands-1 and -2 form tube-like hole surfaces enclosing the $\Gamma - A$ line and closed pockets at the A point. Band-3 forms a complex electron surface, while band-4 consists of cigar-shaped electron pockets located at the Brillouin-zone boundary. As reported in Ref.[SM16], the band-3 Fermi surface undergoes a significant reconstruction upon the introduction of a small Hubbard U . The inclusion of $U = 0.01$ Ry enlarges the volumes of the band-1 and -2 Fermi surfaces and breaks the complex connectivity of the band-3 Fermi surface, generating several small pockets.

To reproduce the experimentally observed oscillation frequency α with the extremal orbit 1-A-o of the band-1 Fermi surface obtained in the DFT+ U calculation, the Fermi levels of bands 1 and 2 were shifted upward by 0.046 eV. For bands 3 and 4, the Fermi level was shifted downward by 0.007 eV to compensate for the associated change in carrier number,

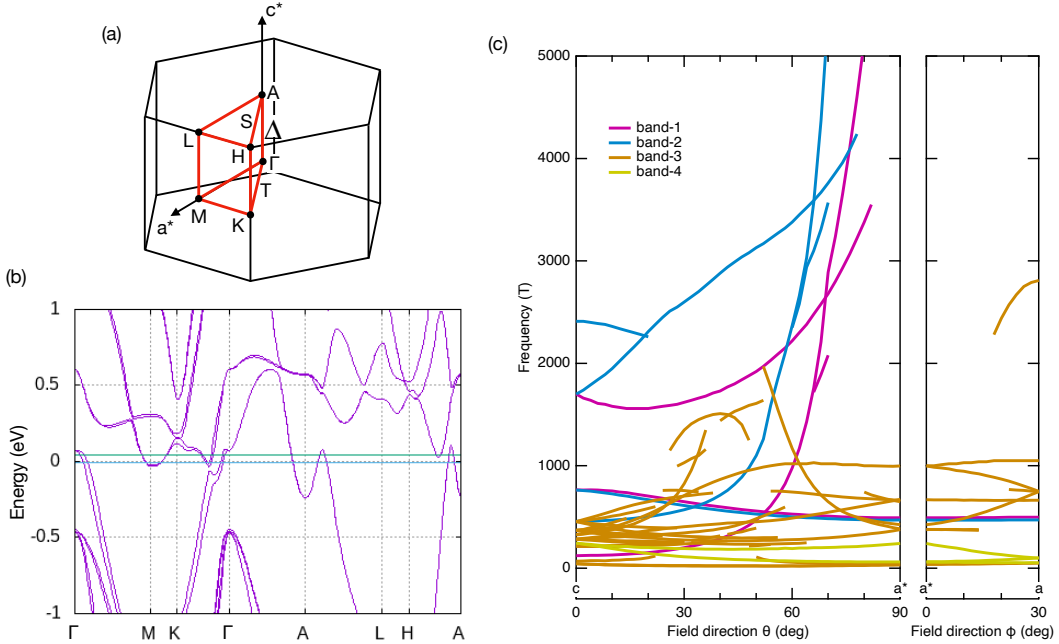


FIG. S 1. (a) Brillouin zone and high-symmetry points. The high-symmetry lines Δ , S, and T are also indicated. The Γ MK, Γ KHA, and ALH planes are nodal planes of altermagnetic spin splitting without spin-orbit coupling. (b) Calculated band structure of CrSb. The original Fermi level is at $E = 0$. The green and light blue horizontal lines show the shifted Fermi level for bands-1 and 2 and that for bands-3 and 4, respectively. (c) Calculated quantum-oscillation frequencies.

which is of order ~ 0.015 per unit cell.

Figures S1(a), (b), and (c) show the Brillouin zone, calculated band structure, and calculated quantum-oscillation frequencies, respectively. Although the calculated Fermi surface is presented in Fig. 2(c), the band-3 Fermi surface is complicated and hence we show its top and side views in Fig. S2.

LANDAU-FAN PLOT OF α OSCILLATIONS

Figure S3 shows the Landau-fan plot of α oscillations for $B \parallel c$ based on the data shown in Fig. 1(a), assigning an integer index n to each ρ_{osc} peak. A linear fitting gives a frequency of $F = 1627$ T, very close to 1628 T determined from a Fourier transform. The n -axis intercept is $-0.06(3)$, which is very close to zero, in contrast to the value of -0.1667 reported in [SM17].

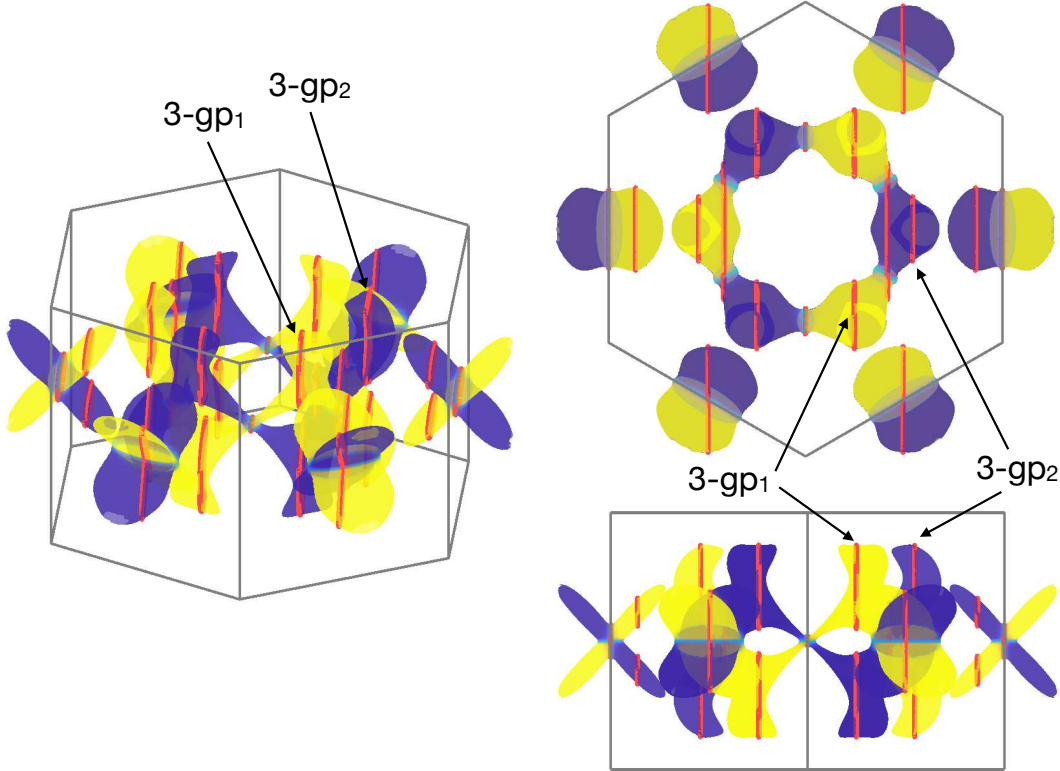


FIG. S 2. Band-3 Fermi surface.

The intercept cannot be straightforwardly interpreted, for the following reasons: First, the value of ϕ_Z in Eq. (S1) is not readily estimated. Second, the oscillation frequency F_1 from the maximum cross-section of the band-1 Fermi surface (orbit 1-A-o) approaches F_2 from the minimum cross-section of band-2 (orbit 2-A-o) in field directions near $B \parallel c$. Therefore the observed α oscillation near $B \parallel c$ is actually a sum of both frequencies and the phase analysis of the α oscillation becomes very ambiguous.

Let us consider how the near-zero intercept that we found can be explained. The experimentally observed oscillation ρ_{osc}^{exp} is the sum of two oscillations:

$$\begin{aligned} \rho_{osc}^{exp} = & -A_1(T, B) \cos \left[2\pi \left(\frac{F_1}{B} - \frac{1}{2} \right) - \frac{\pi}{4} + \phi_{B,1} + \phi_{Z,1} \right] \\ & - A_2(T, B) \cos \left[2\pi \left(\frac{F_2}{B} - \frac{1}{2} \right) + \frac{\pi}{4} + \phi_{B,2} + \phi_{Z,2} \right]. \end{aligned} \quad (S2)$$

F_1 and F_2 are rendered slightly different by spin-orbit coupling and/or slight misorientations of the field direction. As the two orbits are degenerate when spin-orbit coupling is absent and the magnetic field is exactly parallel to the c axis, we assume $A_1 = A_2$, $\phi_{B,1} = -\phi_{B,2}$,

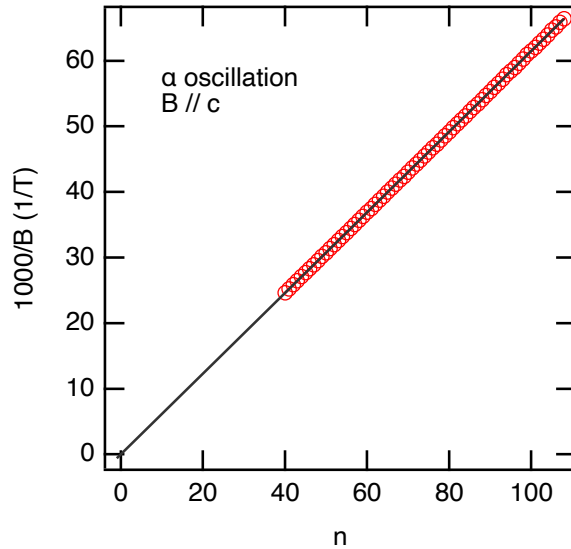


FIG. S 3. Landau fan plot of α oscillations with $B \parallel c$.

and $\phi_{Z,1} = -\phi_{Z,2}$. We then obtain

$$\rho_{osc}^{exp} = -2A_1(T, B) \cos \left(\frac{\Delta F}{B} \pi + \frac{\pi}{4} - \phi_{B,1} - \phi_{Z,1} \right) \cos \left[2\pi \left(\frac{F_{av}}{B} - \frac{1}{2} \right) \right], \quad (S3)$$

with

$$\Delta F = F_2 - F_1 > 0 \text{ and } F_{av} = (F_1 + F_2)/2. \quad (S4)$$

Because the cosine prefactor can be positive or negative depending on ΔF , B , $\phi_{B,1}$, and $\phi_{Z,1}$, the n -intercept also depends on these parameters. If the cosine prefactor is positive within the investigated field range, the n -axis intercept of the Landau-fan plot is zero. For example, the prefactor remains positive in the field range of Fig. S3 when $\Delta F = 5$ T and $\phi_{B,1} + \phi_{Z,1} = \pi/2 \pmod{2\pi}$. In this case, the prefactor is maximized at $B = 20$ T and decreases with increasing B . This trend might explain the slight concavity in the Dingle plot of α in Fig. 3(b). However, even if this assumption is correct, the Berry phase $\phi_{B,1}$ cannot be uniquely determined.

Under the assumption of Eq. (S3), determination of the Berry phase requires observing multiple zero-crossing fields of the prefactor to fix the sum $\phi_{B,1} + \phi_{Z,1}$. Furthermore, $\phi_{Z,1}$ must be independently determined.

TABLE S I. Experimental Fermi surface parameters of CrSb for $B \parallel c$, a^* , and a . Data for the δ frequency at $\theta = -60^\circ$, where the effective mass was determined, are also shown. The right side shows the theoretical candidate orbits, named by their band number, orbit center, and (if necessary) inner (i) or outer (o). T denotes a point on the high-symmetry line Γ K.

Field		Experiment				Calculation		
direction	Branch	F (kT)	m^*/m_e	τ (ps)	μ (cm ² /(Vs))	Orbit	F (kT)	m_{band}/m_e
$B \parallel c$	α	1.63	1.2(1)	0.38(4)	560(30)	1-A-o	1.70	0.81
	δ	0.74				2-A-o	1.70	0.81
						1-A-i	0.76	0.58
						2-A-i	0.76	0.58
$B \parallel a^*$	β	0.77	1.23(5)	0.28(2)	400(20)	3-gp ₁	0.67	0.70
	ϵ	0.11	0.29(3)	0.11(3)	700(100)	4-M	0.06	0.48
	ζ	0.04				3-T	0.04	0.25
$B \parallel a$	β	0.78				3-gp ₁	0.66	0.64
	ϵ	0.14				4-M	0.10	0.79
	ζ	0.05	0.24(1)			3-T	0.05	0.35
$\theta = -60^\circ$	δ	0.47	1.2(2)			3-gp ₂	0.49	0.96

EXPERIMENTAL AND CALCULATED FERMI SURFACE PARAMETERS OF CrSb

Table SI shows the experimental frequencies, effective masses, electron scattering times τ , and mobilities μ for $B \parallel c$, a^* , and a , along with the theoretical candidate frequencies for comparison and the data of the δ branch at $\theta = -60^\circ$.

* TERASHIMA.Taichi@nims.go.jp

† Present address: Department of Physics, Tokyo Metropolitan University, 1-1, Minami-
osawa, Hachioji 192-0397, Japan

‡ urata.takahiro.k4@f.gifu-u.ac.jp; Present address: Department of Electrical, Electronic and
Computer Engineering, Gifu University, Gifu, Gifu 501-1193, Japan

§ ikedah@fc.ritsumei.ac.jp

- [SM1] T. Urata, W. Hattori, and H. Ikuta, High mobility charge transport in a multicarrier altermagnet CrSb, *Phys. Rev. Mater.* **8**, 084412 (2024).
- [SM2] X. Peng, Y. Wang, S. Zhang, Y. Zhou, Y. Sun, Y. Su, C. Wu, T. Zhou, L. Liu, H. Wang, J. Yang, B. Chen, Z. Fang, J. Du, Z. Jiao, Q. Wu, and M. Fang, Scaling behavior of magnetoresistance and Hall resistivity in the altermagnet CrSb, *Phys. Rev. B* **111**, 144402 (2025).
- [SM3] F. E. Richards, Investigation of the magnetoresistance quantum oscillations in magnesium, *Phys. Rev. B* **8**, 2552 (1973).
- [SM4] D. Shoenberg, *Magnetic Oscillations in Metals* (Cambridge University Press, Cambridge, 1984).
- [SM5] G. P. Mikitik and Y. V. Sharlai, Semiclassical energy levels of electrons in metals with band degeneracy lines, *Soviet Physics–JETP* **87**, 747 (1998).
- [SM6] A. Alexandradinata and L. Glazman, Fermiology of topological metals, *Annu. Rev. Condens. Matter Phys.* **14**, 261 (2023).
- [SM7] H. Aoki, N. Kimura, and T. Terashima, Fermi surface properties, metamagnetic transition and quantum phase transition of CeRu_2Si_2 and its alloys probed by the dHvA effect, *J. Phys. Soc. Jpn.* **83**, 072001 (2014).
- [SM8] P. Blaha, K. Schwarz, F. Tran, R. Laskowski, G. K. H. Madsen, and L. D. Marks, WIEN2k: An APW+lo program for calculating the properties of solids, *J. Chem. Phys.* **152**, 074101 (2020).
- [SM9] J. P. Perdew, K. Burke, and M. Ernzerhof, Generalized Gradient Approximation Made Simple, *Phys. Rev. Lett.* **77**, 3865 (1996).
- [SM10] W. J. Takei, D. E. Cox, and G. Shirane, Magnetic structures in the MnSb-CrSb system, *Phys. Rev.* **129**, 2008 (1963).
- [SM11] A. I. Liechtenstein, V. I. Anisimov, and J. Zaanen, Density-functional theory and strong interactions: Orbital ordering in Mott-Hubbard insulators, *Phys. Rev. B* **52**, R5467 (1995).
- [SM12] A. B. Shick, A. I. Liechtenstein, and W. E. Pickett, Implementation of the LDA+U method using the full-potential linearized augmented plane-wave basis, *Phys. Rev. B* **60**, 10763 (1999).
- [SM13] A. G. Petukhov, I. I. Mazin, L. Chioncel, and A. I. Lichtenstein, Correlated metals and the LDA + U method, *Phys. Rev. B* **67**, 153106 (2003).

[SM14] N. Marzari and D. Vanderbilt, Maximally localized generalized Wannier functions for composite energy bands, *Phys. Rev. B* **56**, 12847 (1997).

[SM15] J. Kuneš, R. Arita, P. Wissgott, A. Toschi, H. Ikeda, and K. Held, Wien2wannier: From linearized augmented plane waves to maximally localized Wannier functions, *Comput. Phys. Commun.* **181**, 1888 (2010).

[SM16] C. Li, M. Hu, Z. Li, Y. Wang, W. Chen, B. Thiagarajan, M. Leandersson, C. Polley, T. Kim, H. Liu, C. Fulga, M. G. Vergniory, O. Janson, O. Tjernberg, and J. van den Brink, Topological Weyl altermagnetism in CrSb, *Commun. Phys.* **8**, 311 (2025).

[SM17] J. Du, X. Peng, Y. Wang, S. Zhang, Y. Sun, C. Wu, T. Zhou, L. Liu, H. Wang, J. Yang, B. Chen, C. Xi, Z. Jiao, Q. Wu, and M. Fang, Topological nontrivial Berry phase in altermagnet CrSb, arXiv:2509.21303 (2025).